JOURNAL OF AIRCRAFT
Vol. 48, No. 2, March–April 2011

Stress in Triple-Row Riveted Lap Joints Under the Influence of Specific Factors

Gang Li,* Guoqin Shi,† and Nicholas C. Bellinger‡
National Research Council Canada, Ottawa, Ontario K1A 0R6, Canada

DOI: 10.2514/1.C031129

Effects of fastener clearance fit, friction coefficient, and corrosion pillowing on the stress state in triple-row riveted lap joints were studied numerically using three-dimensional finite element methods. The material elastoplastic constitutive relationship and geometric nonlinear properties, as well as nonlinear contact boundary conditions, were included in the numerical simulations. The numerical modeling was validated using experimental measurements of the rivet driven-head deformation and in situ strains. The lap joints were loaded in tension after riveting. Three different clearance fits, three different friction coefficients, and four corrosion-pillowing conditions were analyzed. The stress variations along prescribed paths and full-field contours of the maximum principal stress on joint faying surfaces during the tensile loading stage were investigated. Insightful results of the stress state in riveted lap joints were obtained, which could effectively explain the phenomena observed from joint fatigue tests. The phenomena include 1) the potential major factor to cause the joint fatigue-life scatter, 2) crack-nucleation site location in the top rivet-hole vicinity on the outer-sheet faying surface for the noncorroded joints, and 3) the occurrence of the multiple-site damages in aged and corroded lap joints.

Nomenclature

A = cross-sectional area of rivet shank
C = material parameter
D = rivet shank diameter
D_{hole} = protruding-hole diameter
$D_{\max}$ = maximum diameter of the rivet driven head after riveting
L = joint length
m = material parameter
R^2 = data fit parameter
t = joint sheet thickness
ε = normal strain
$\varepsilon_{\mathrm{true}}$ = true strain
σ = normal stress
σ_{NRSS} = nominal rivet squeeze stress
σ_{true} = true stress
σ_y = initial yield stress

I. Introduction

TRIPLE-ROW countersunk riveted lap joints, commonly used in aircraft fuselage structures, are subjected to combined loadings from fuselage internal pressurization and secondary bending due to the tensile load path eccentricity. The stress condition is further complicated by stress concentrations in the fastener-hole region, due to the existence of the countersunk holes, and residual stresses around the hole induced by the riveting process [1–6]. The magnitude of the induced residual stress is directly dependent on the rivet squeeze force [1,3,4]. A large compressive residual stress in the hole vicinity is created by a large rivet squeeze force (RSF), which can greatly improve the joint fatigue life [1,4,5]. Test results have shown that a certain degree of scatter is present in the fatigue life for the riveted lap joints under the same loading condition [7,8]. The causes of this scatter could be attributed to differences in the clearance fit between the rivet and the fastener-hole edge, knife edge hole conditions in the outer sheet, corrosion pillowing between overlap regions, fastener-hole conditions, scatter in the material property, riveting condition, etc. By properly selecting the rivet size and/or panel thickness, a knife-edge hole can be avoided. The most controllable factor during the manufacturing process should be the clearance fit. When riveted lap joints are subjected to cyclic loading conditions, fretting damage can lead to rough faying surfaces resulting in an increase in the friction coefficient. This large friction coefficient could, in turn, increase the degree of fretting damage. Inevitably, corrosion combined with fatigue damage can form in aircraft, which could lead to catastrophic failure of a structure. The buildup of corrosion products can cause out-of-plane deformations, i.e., pillowing, in the lap-joint overlap region, which can significantly increase the stress in lap joints.

Previously, a project on the study of corrosion and its effect in fuselage lap joints of transport aircraft was conducted at the Institute for Aerospace Research. A mathematical model was developed to correlate the pillowing deformation to the degree of corrosion present in a joint [9]. Pillowing was simulated using out-of-plane internal pressures caused by the corrosion within the overlap region. Three-dimensional linear finite element methods were carried out to study this effect on lap joints. The actual riveting process was not included and the rivet driven-head dimension was artificially set in the finite element (FE) models. The rivet clamp-up pressure was introduced by applying self-equilibrated compressive stress to the two rivet ends. Insightful results about the stress condition were obtained [8–12]. Then, a follow up project was initiated to develop numerical modeling and methodologies to study the riveting process and its effect on riveted lap joints. Effects of the riveting process on the residual stress/strain in joints were studied experimentally and numerically [13–15]. Two-dimensional nonlinear FE methods were used to simulate the actual riveting process, and insightful information on the residual stress/strain distribution and driven-head dimension versus the applied rivet squeeze force was obtained

---

Presented as Paper 2010-3025 at the 51st AIAA/ASME/ASCE/AHS/ASC Structures, Structural Dynamics, and Materials Conference, Orlando, FL, 12–15 April 2010; received 4 June 2010; revision received 7 December 2010; accepted for publication 7 December 2010.

*Associate Research Officer, Structures and Materials Performance Laboratory, Institute for Aerospace Research, 1200 Montreal Road; Gang.Li@nrc-cnrc.gc.ca. Member AIAA (Corresponding Author).

†Senior Research Officer, Structures and Materials Performance Laboratory, Institute for Aerospace Research, 1200 Montreal Road. Member AIAA.

‡Structures Group Leader, Principal Research Officer, Structures and Materials Performance Laboratory, Institute for Aerospace Research, 1200 Montreal Road. Member AIAA.

[14,15]. The effect of the residual stress on the stress variation during tensile loading for countersunk riveted lap joints was successfully studied using 3-D FE methods with the aid of relevant experimental tests [16,17]. Both the riveting process and the tensile loading stage were included in these 3-D FE analyses. The material elastoplastic constitutive relationship and geometric nonlinear properties, as well as nonlinear contact boundary conditions, were included in the numerical models [14–17].

A literature review [1–17] showed that there was little quantitative study available on the effect of clearance fit and friction coefficient on the stress/strain variation in triple-row countersunk riveted lap joints. Furthermore, an accurate numerical analysis of the corrosion-pillowing effect on the stress state in lap joints is also needed. To this end, the effects of fastener clearance fit, friction coefficient, and corrosion pillowing on the stress condition in the fastener-hole vicinity was studied in this paper.

In this study, three different squeeze forces were used to install the rivets. After riveting, the lap joints were loaded in tension to a maximum remote stress of 98.6 MPa [16,17]. Rivet driven-head deformation and measured strain were used to validate the numerical modeling. Then, a parametric study was carried out using the validated 3-D nonlinear finite element methods to address issues that could not be looked into directly in the experimental tests. The main objective of this work was to accurately quantify the stress state in riveted lap joints under key factors for further use of the obtained stress information to explain existing fatigue data and relevant phenomena and then to improve the prediction capability on the fatigue life of fuselage lap joints.

II. Experimental Details

A. Joint and Strain-Gauge Information

A total of three strain-gauged lap-joint specimens were tested in the validation stage for an accurate numerical modeling methodology. Triple-row countersunk riveted 25.4-mm-wide lap joints were prepared. Each joint consisted of two 1.60-mm-thick bare 2024-T3 Al alloy sheets, riveted with three Al 2117-T4 alloy countersunk-type MS20426AD5-6 rivets. Joint configuration and dimensions are given in Fig. 1. The total joint length L was 337.72 mm. Tabs with dimensions of 50 × 25.4 × 1.60 mm were clamped with the ends of each joint to eliminate the initial secondary bending moment that would be induced when the joints were installed in the load frame. The rivet protruding height H_o was 6.06 mm. Based on the optical measurements of nine holes in three lap joints, the sheet mean protruding-hole diameter D_{hole} was approximately 4.09 mm, the maximum and minimum values of the sheet protruding-hole diameter were approximately 4.09 and 4.07 mm. The rivet shank diameter D was 3.97 mm, and the mean radial clearance fit between the rivet and protruding hole was calculated to be 0.06 mm.

Microstrain gauges were used to capture the strain variations during the test [13–17]. All the microstrain gauges pointed in the longitudinal (tensile) direction, as shown in Fig. 1. The global coordinate-frame origin was set at the middle fastener-hole center. Strain gauges 1 to 4 were mounted on the inner-sheet surface before riveting in order to capture the strain variation during the riveting process. Strain gauges 5 to 7 were mounted after riveting. Microstrain gauges 1 to 3 were type MM EA-13-031DE-350 with a gauge factor of 2.06 ± 1.0% and transverse sensitivity of (1.2 ± 0.2)% at 24°C. Microstrain gauges 4 to 7 were type MM EA-13-031EC-350 with a gauge factor of 2.09 ± 1.0% and transverse sensitivity of (0.4 ± 0.2)% at 24°C. Gauges 1 to 3 were used to measure the strain values in the hoop direction, and gauge 4 was used to measure the radial strain during the riveting process. All the gauges were reset to zero and then used to measure the longitudinal strain variations during the tensile loading stage. Secondary bending, at the overlap end, was estimated from the strain values in gauges 5 and 6. Gauge 7 was used to measure the far-field strain.

To avoid possible damage to the strain gauges by the large rivet driven-head deformation and difficulties in gauge setup, gauges 1 to 4 were mounted more than 2.5 mm away from the hole edge. Table 1

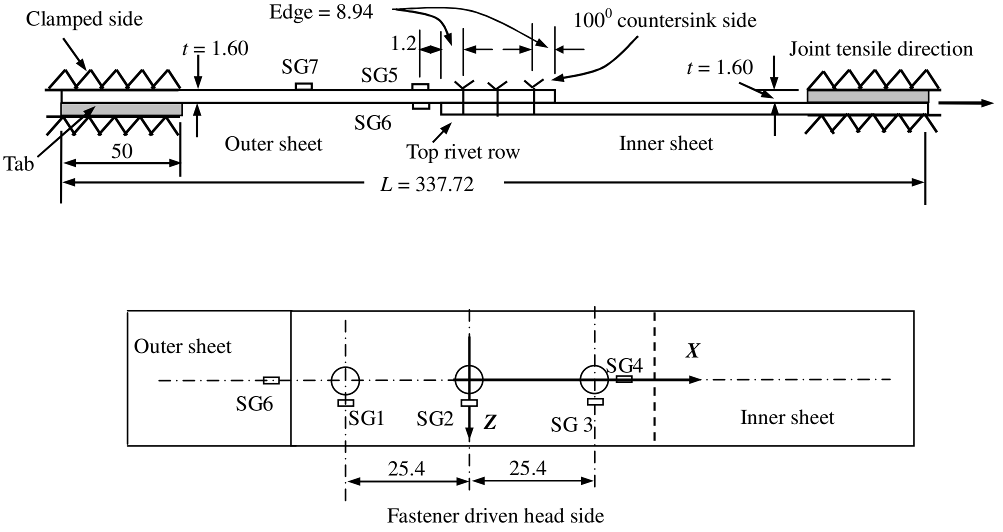

a) Triple-row riveted lap joint and the strain gauge arrangement (not to scale)

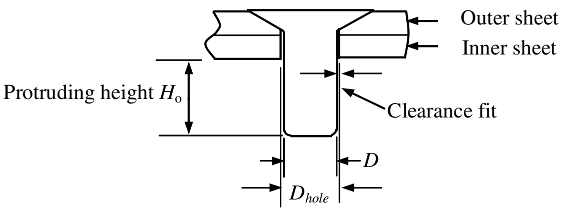

b) Countersunk rivet before riveting process

Fig. 1 Schematic diagrams of the 25.4-mm-wide lap joint with the microstrain-gauge arrangement and the rivet configuration before the riveting process (dimensions are in millimeters).

Table 1 Locations of microstrain gauges 1 to 7 (Fig. 1)

Gauge[a]	Parameters	Value, mm
Inner-sheet surface (mounted before riveting)		
Gauge 1	*z* position (±0.4) (absolute value)	6.1
Gauge 2	*z* position (±0.4) (absolute value)	6.2
Gauge 3	*z* position (±0.4) (absolute value)	6.5
Gauge 4	*x* position (±0.4)	6.5
Outer-sheet surface (mounted after riveting)		
Gauge 5	Distance to the overlap edge	1.2
Gauge 6	Distance to the overlap edge	1.2
Gauge 7	Distance to the overlap edge	42

[a] The gauge length was around 0.8 mm. The positions of strain gauges 1 to 4 were measured between the adjacent hole center and the gauge center, and the positions of strain gauges 5 to 7 were identified relatively to the adjacent overlap end.

gives these microstrain-gauge locations. The positions of the strain gauges 1 to 4 were identified relatively to their nearby local fastener-hole centers, and the positions of the strain gauges 5 to 7 were measured relative to the overlap end. Since the gauges were not located within the hole vicinity and the joint maximum remote tensile stress was less than one third of the sheet initial yield stress, the measured strains were much less than the strain-gauge limit of approximately 3%. Thus, the influences of the gauge transverse sensitivity and nonlinearity on the measured strains were not considered. Each strain-gauged specimen was tested using one of the three different rivet squeeze forces of 10, 14, and 18 kN.

B. Testing Equipment and Loading Condition

Lap-joint specimens were riveted and then loaded in tension using a 250 kN MTS load frame. To avoid both thermal and inertial effects on the material properties, a small constant load ramp of 111.2 N/s was chosen for all the rivet installations [13–17]. This rate is much slower than that used in the actual riveting process. The three rivets were installed one by one starting from the center rivet. To keep the same riveting condition for each coupon, the coupons were held firmly to a mobile heavy metal plate. The gauges were reset to zero before the next riveting process to avoid any potential disturbances to both gauges and coupon. After riveting, the joints were loaded in tension to a maximum remote stress of 98.6 MPa. The tensile loading rate was 0.5 mm/ min.

III. Finite Element Simulations

A. Finite Element Modeling

The FE model was generated in accordance with the experimental joints using the FE software packages MSC.Patran (pre- and postprocessor) version 2005r2 and MSC.Marc version 2005 (solver). Because of the joint symmetry, only half of the joint was modeled. A total of 12,362 nodes and 9096 eight-node three-dimensional reduced-integration brick elements (type 117) were used. The meshed overlap region of the lap joint is shown in Fig. 2. Symmetric boundary conditions were applied to the joint center plane along the longitudinal *x* direction. Joint displacement boundary and loading conditions were the same as that of the experimental tests. Element type 117 is an eight-node isoparametric arbitrary hexahedral for general three-dimensional applications using reduced integration, which is preferred over high-order elements when used in a contact analysis [18].

Five deformable contact bodies, two sheets and three rivets, four rigid contact bodies, three pushers to squeeze the rivet driven-heads, and one rigid set contacting the joint bottom surface during the riveting process were defined in the model. Multiple load steps with their specific boundary conditions were defined in the loading sequence. Load steps 1 and 2 applied the squeeze force to the center pusher to squeeze the center rivet and then released the squeeze force to 0; load steps 3 and 4 applied the squeeze force to the top rivet pusher to install the top rivet and then released the squeeze force to 0; load steps 5 and 6 did the same to the lower fastener; and load step 7 applied the in-plane loading to the joint, up to a maximum stress of 98.6 MPa. In the final load step, the three deformable bodies contacted each other while the rigid bodies were deactivated. A friction coefficient of 0.2 was used in the Coulomb friction law for all contact surfaces [4]. A force-controlled riveting method was used in this numerical study. The same squeeze force was used to install all three rivets in the joint. Details on the displacement boundary conditions, and contact pairs in each load case are fully described elsewhere [17].

B. Material Parameters

The material parameters used were the same as those used in [13–17]. An isotropic hardening behavior was assumed for both the rivet and sheet materials. The material constants *C* and *m* were calculated by substituting the uniaxial tensile test data into Eq. (1).

$$\sigma_{\mathrm{true}} = C(\varepsilon_{\mathrm{true}})^m \tag{1}$$

The true stress and plastic strain values were entered into MSC.Patran, which uses linear interpolation for values between the points to implement the hardening behavior in the model. The material parameters for the 2117-T4 Al alloy MS20426ADx-x rivet [4,13–17,19] and bare 2024-T3 Al alloy sheet [13–17,19] are summarized in Tables 2 and 3, respectively.

IV. Results and Discussion

A. Comparison of Experimental and Numerical Results

1. Joint Deformation

To eliminate the influence of the rivet dimensions, the normalized variation of the rivet driven-head deformation, $D_{\max}/D$, versus the nominal rivet squeeze stress (NRSS), was determined in previous riveting tests. Three different single-riveted-joint cases were considered, and four different rivet squeeze forces were used for each case. The three different joint cases were 1) countersunk-type MS20426AD6-7 rivets with 1.60-mm-thick clad 2024-T3 Al alloy sheets, 2) MS20426AD8-9 rivets with 2.03-mm-thick bare 2024-T3

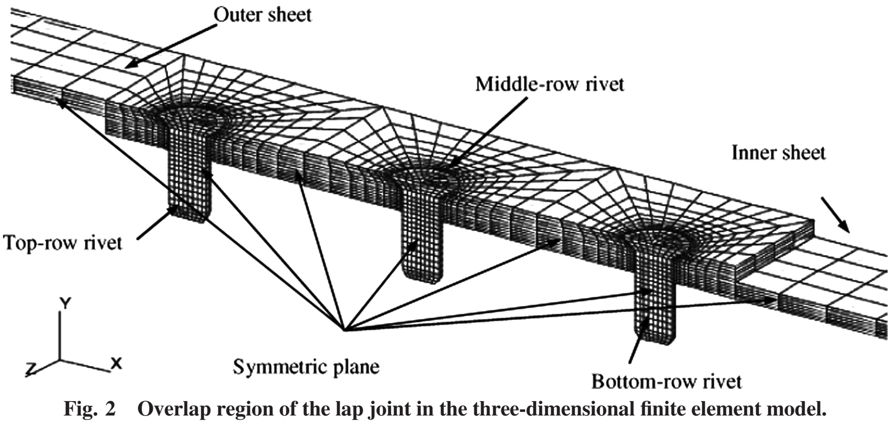

Fig. 2 Overlap region of the lap joint in the three-dimensional finite element model.

Table 2 Elastic and plastic properties for MS20426AD5-6 rivet material

Parameter of rivet	Value
Young's modulus	71.7 GPa
Poisson's ratio	0.33
Initial yield stress, σ_y	172 MPa
Hardening parameters when $0.02 \le \varepsilon_{\text{true}} \le 0.1$	$C = 544$ MPa and $m = 0.23$
Hardening parameters when $0.1 < \varepsilon_{\text{true}} < 1.0$	$C = 551$ MPa and $m = 0.15$

Table 3 Material parameters for 1.60-mm-thick bare 2024-T3 Al alloy sheet

Parameter of bare 2024-T3 Al alloy sheet	Value
Young's modulus	72.4 GPa
Poisson's ratio	0.33
Initial yield stress σ_y	310 MPa
True ultimate stress	552 MPa
Hardening parameters for $\varepsilon_y \le \varepsilon_{\text{true}} \le 0.02$	$C = 676$ MPa and $m = 0.14$
Hardening parameters for $0.02 < \varepsilon_{\text{true}} \le 0.1$	$C = 745$ MPa and $m = 0.164$
Slope of linear hardening curve for $\varepsilon_{\text{true}} > 10\%$	1034 MPa

Al alloy sheets, and 3) MS20426AD8-9 rivets with 2.11-mm-thick clad 2024-T3 Al alloy sheets. Variations in the three sets of rivet driven-head deformations versus rivet squeeze stress could be estimated using the following regression expression:

$$\frac{D_{\max}}{D} = 1.433\sigma_{\text{NRSS}}^{0.3322} \qquad (R^2 = 0.99) \tag{2}$$

where D is the rivet shank diameter, $D_{\max}$ is the rivet maximum deformed shank diameter, and R^2 is a data fit degree indicator. The power-law regression equation is valid for nominal rivet squeeze stress σ_{NRSS} within the range of 0.75–1.75 GPa, expressed without the gigapascal dimension. The corresponding NRSS is defined in Eq. (3):

$$\sigma_{\text{NRSS}} = \text{RSF}/A \tag{3}$$

where RSF is the rivet squeeze force, and A is the cross-sectional area of the rivet shank.

Rivet driven-head deformations in the MS20426AD5-6 rivet obtained from the experimental and numerical results using the 18 kN RSF are shown in Fig. 3. Comparisons of this rivet driven-head deformations are summarized in Table 4. Large rivet squeeze forces induced large driven-head deformations. Good agreement was achieved for the rivet driven-head deformation from the numerical simulations. The relative difference in the rivet driven-head deformation, $D_{\max}/D$, was within 2.3% between the experimental results and regression prediction [Eq. (2)] and 2% between the experimental and FE results. Because of the elimination of the dimensional effects, the regression expression of Eq. (2) could be used to predict the rivet driven-head deformation of rivets of different dimensions.

Table 4 Rivet driven-head deformation obtained from current experimental tests, regression expression in Eq. (3), and FE analysis results

		$D_{\max}/D$		
RSF, kN	Stress, GPa	Current test	Equation (2)	FE
10	0.81	1.31	1.34	1.32
14	1.13	1.50	1.50	1.52
18	1.46	1.63	1.63	1.66

2. *In Situ Quantitative Comparisons During the Riveting Process*

Because of the distance between the rivets, the riveting process did not influence the adjacent holes. For comparison purposes, the experimental average hoop strains for gauges 1 to 3 ($\varepsilon_{\text{avg}} = (\varepsilon_{G1} + \varepsilon_{G2} + \varepsilon_{G3})/3$) were used because the holes were located at similar positions relative to each other. Comparisons of the average hoop strain from gauges 1 to 3 and the radial strain from gauge 4 during the riveting process are presented in Fig. 4. The tensile hoop strain and the compressive radial strain were measured during the riveting process. A small elastic recovery was observed in the radial direction from the numerical simulations. A similar trend, without the evident strain reversal, can be observed from the experimental results. The reversal strain occurred in previous test results [16], which could have resulted from the clearance that was present between the sheet/rivet-hole interface and the rivet standing position (distance of rivet head above sheet surface) during the riveting process. Generally, the difference between the numerical predictions and experimental results is smaller after riveting. For example, a larger difference in gauge 4 (radial strain) is observed in the middle rivet squeezing period than from the initial and final rivet squeezing down periods, but the final difference is less than 10% after riveting.

3. *In Situ Quantitative Comparisons During the Tensile Loading Stage*

Quantitative strain comparisons, during the tensile loading stage, were carried out after the riveting process to further validate the numerical results. The experimentally measured residual strains were used as the starting values for the strain variations in gauges 1 to 4 during the tensile loading stage. For the strain gauges 5 to 7, mounted after riveting, the zero residual strain was the starting value during the tensile loading stage.

a. Strain Variations in the Joint Overlap Region. Good correlation was achieved in all the strain gauges, as shown in Fig. 5.

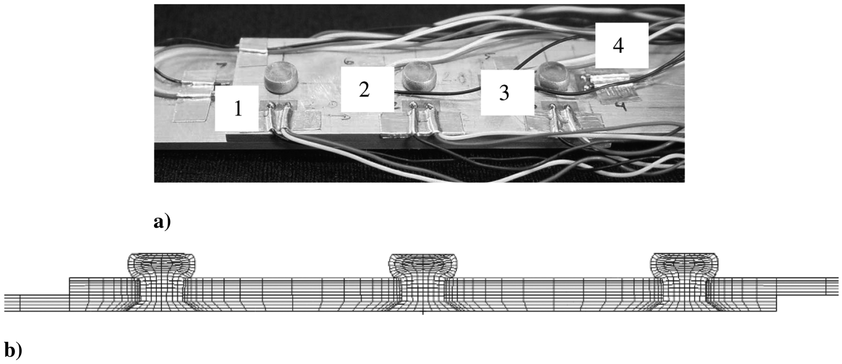

Fig. 3 MS20426AD5-6 rivet driven-head deformations in the lap joint after the riveting process using the 18 kN rivet squeeze force obtained from a) experimental and b) FE results.

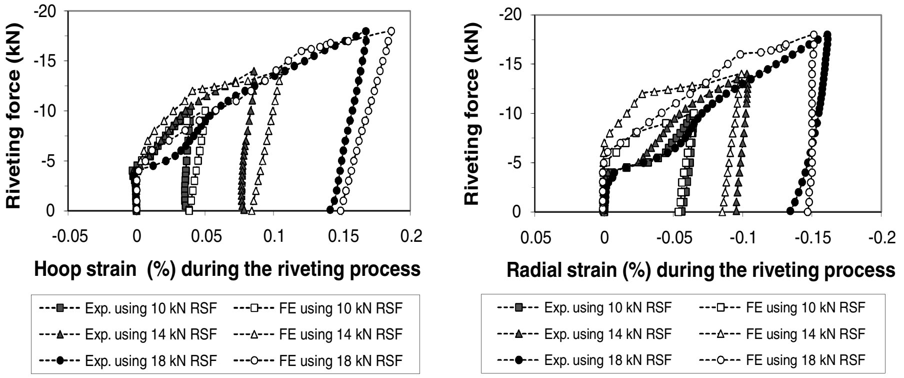

a) Average hoop strain of strain gauges 1 to 3 **b) Radial strain in strain gauge 4**

Fig. 4 Comparison of the variations of the hoop and radial strains on the joint inner surface during the riveting process using the three different RSFs.

Gauge 1 was on the inner sheet near the top-row rivet and showed that the tensile hoop strain initially increased and then slightly decreased with increasing tensile load (Fig. 5a). This result was dominantly influenced by the secondary bending. The trends obtained from the experimental and numerical results in gauge 3 were fairly good with the softer joints in the FE models than with the actual joints. The reason for this discrepancy could be the numerical error in dealing with secondary bending and the contact between the rivets and the sheets.

b. Strain Variations at the Joint Overlap End and Remote Position. Strain gauges 5 and 6 were mounted near the joint overlap to estimate the secondary bending moment when the joint was in tension. As shown in Fig. 6a, the bending strain, $(\varepsilon_{G6} - \varepsilon_{G5})/2$, at that location slightly decreased with increased rivet squeeze forces. The bending strains at that cross-sectional section were approximately 0.06225, 0.05352, and 0.04926% for the joints in tension up to 98.6 MPa remote stress after their specific riveting processes using the 10, 14, and 18 kN forces, which showed that large rivet squeeze force could increase the integrity for the joint structures. Good agreement was achieved between the experimental and FE result for each specific riveting condition. For clarity, only the FE results for the joint riveted using the 18 kN force were plotted with these experimental results. The relative errors between the numerical and experimental strain results increased with the increment of remote force, and the maximum errors were approximately 10% in gauge 5 and 6% in gauge 6, when the remote tensile stress was 98.6 MPa.

The longitudinal remote strain variations in gauge 7 for the three joints are plotted in Fig. 6b. These experimental results were almost identical and correlated well with the FE results. For clarity, only one set of FE results were used to compare with experimental data. The remote strain was within the elastic range of the material and the rivet squeeze force did not influence the joint remote strain variations.

c. Discussion. Generally, good agreement was achieved between the experimental and numerical results in both rivet driven-head deformation and strain variations. It could be drawn from these

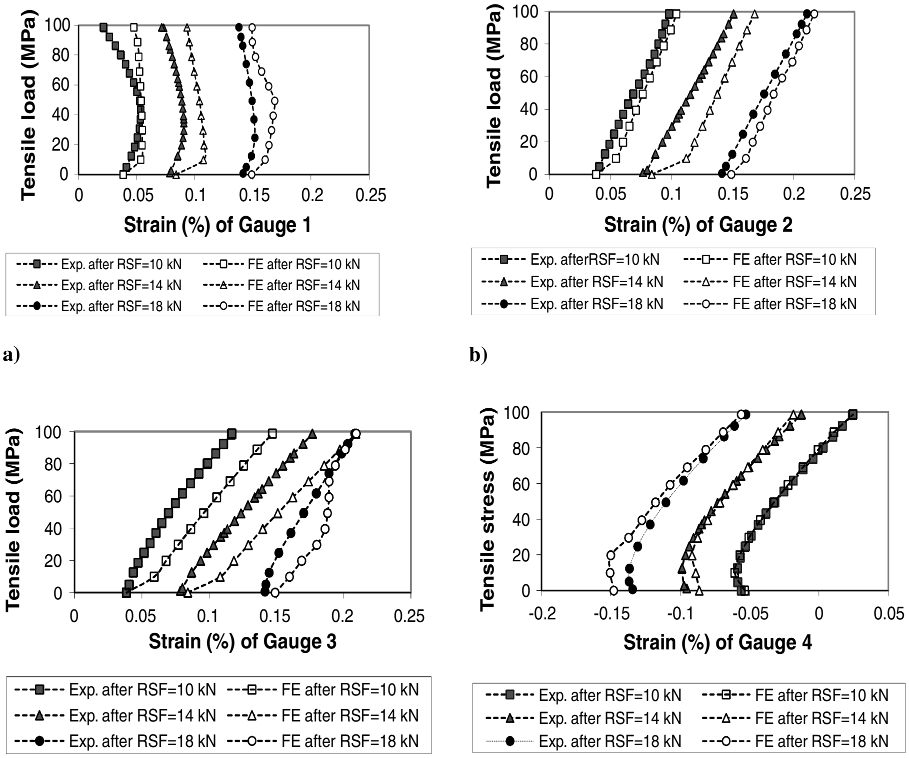

a) b)

c) d)

Fig. 5 Comparison of the longitudinal strain variations in strain gauges 1 to 4 joints during the tensile loading stage after riveting using the three different RSFs.

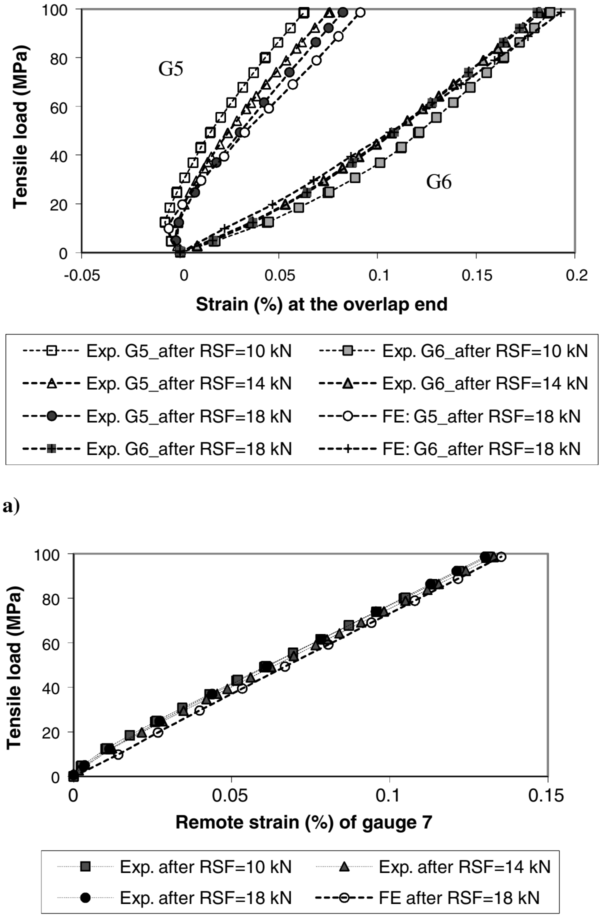

a)

b)

Fig. 6 Comparison of the strain variations in a) strain gauges 5 and 6 at the overlap end and b) strain gauge 7 at the remote position during the tensile loading stage after releasing the three different rivet squeeze forces.

strain comparisons that the stress condition, in riveted lap joints, could be analyzed using the current numerical methods with reasonable accuracy.

The discrepancy between the experimental and FE method predictions could be explained by the following: 1) inaccuracies in the constitutive models beyond yielding for the sheet and rivet used in the model; 2) perfect assumptions made for the material properties and perfect geometry surfaces; 3) differences in how the strain values were obtained: the strain was determined from a point/node in the FE model, whereas it was averaged over the gauge area in the experiments; 4) numerical errors in the FE model, etc.

B. Parametric Study of Various Effects on the Stress State in the Lap Joint

Three additional factors were studied: 1) clearance fit between the sheet/rivet interface, 2) friction coefficient, and 3) corrosion pillowing. As listed in Tables 5–7, two additional clearance fits of 0.12 mm and 0.18 mm were considered along with the initial value of 0.06 mm. An identical clearance fit was introduced into three fastener holes for each joint. Two additional friction coefficients of 0.4 and 0.6 were considered in addition to the initial value of the 0.2, and four different corrosion-pillowing conditions were studied in the initial FE model with the 0.06 mm clearance and 0.2 friction coefficient. For the study on the clearance fit and friction coefficient, only the joint riveted using the 18 kN force was numerically evaluated.

For the corrosion study, pillowing pressure was introduced to the faying surfaces after the riveting process stage, before the joint was loaded in tension. A total of four different uniform pillowing pressures of 0.317, 0.634, 0.951, and 1.269 MPa were applied to the pitch areas, between the top- and bottom-row rivet centers. Tapered pillowing pressures, varying linearly from 0 at both overlap ends to uniform at the neighboring fastener-hole center position, were applied, as presented in Fig. 7. The relationship between the material loss caused by corrosion and the pillowing pressure can be found elsewhere [9]. The four nonzero internal pressures in Table 7 were induced by relative sheet-thickness losses of 2.5, 5, 7.5, and 10%.

1. *Hoop-Stress Variations Along Prescribed Transverse Path*

In fatigue tests of noncorroded joints, cracks typically originate in the outer-sheet heavily fretted area around the top rivet hole, a short distance away from the hole edge [7]. Thus, it was decided to study the effects of 1) the clearance fit and 2) the friction coefficient on the hoop-stress variation at the top-row rivet along a transverse path on the outer-sheet faying surface. This path is perpendicular to the joint longitudinal tensile direction. For clarity, the effect of the rivet squeeze force was also considered with the above effects. As shown in Fig. 8a, large rivet squeeze forces increased the magnitude of the compressive residual hoop stress at the hole-edge vicinity and moved the peak tensile stress a short distance away from the hole edge. The maximum residual compressive hoop stress was at the hole edge with the value of −138.73 MPa for the 10 kN RSF, −160.71 MPa for the 14 kN RSF, and −206.95 MPa for the 18 kN RSF. The peak tensile stresses are close to each other with an approximate value of 90 MPa. The effects of the rivet squeeze force, clearance fit, and friction coefficient on the hoop stress for the joint loaded in tension are presented in Figs. 8b–8d.

For a joint remote tensile stress of 98.6 MPa (Fig. 8b), the hoop stress at the hole edge was approximately 40 MPa for the 10 kN RSF riveted joint, −57.8 MPa for the 14 kN RSF riveted joint, and −69.2 MPa for the 18 kN RSF riveted joint.

A significant influence of the clearance fit on the hoop stress can be noted from Fig. 8c for both the edge stress and the peak stress in the hole vicinity. Information on the stress at the hole edge and peak position is summarized in Table 8. It can be seen from Fig. 8c and Table 8 that a large clearance fit of 0.18 mm can completely counteract the benefit induced by the riveting process using the large RSF of the 18 kN. The distance between the location of the maximum

Table 5 Parametric study analysis of case 1: effect of mean radial clearances using the friction coefficient of 0.2

Condition	Mean radial clearance, mm	Rivet squeeze force, kN	Notes
Clearance 1	0.06	10, 14, and 18	Done in initial analysis
Clearance 2	0.12	18	New analysis
Clearance 3	0.18	18	New analysis

Table 6 Parametric study analysis of case 2: effect of friction coefficient under the clearance 1 condition

Condition	Friction coefficient μ	Rivet squeeze force, kN	Notes
Coefficient 1	0.2	10, 14, and 18	Done in initial analysis
Coefficient 2	0.4	18	New analysis
Coefficient 3	0.6	18	New analysis

Table 7 Parametric study analysis of case 3: effect of corrosion pillowing under conditions of clearance 1 and 0.2 friction coefficient

Condition	Applied pillowing pressure, MPa[11]	Rivet squeeze force, kN	Notes
PS0	0	10, 14, and 18	Done in initial analysis
PS1	0.317	10, 14, and 18	
PS2	0.634	10, 14, and 18	New analysis
PS3	0.951	10, 14, and 18	
PS4	1.269	10, 14, and 18	

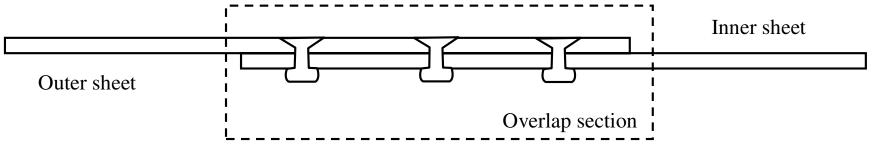

a) Longitudinal cross-sectional area along the joint axis of a riveted lap joint

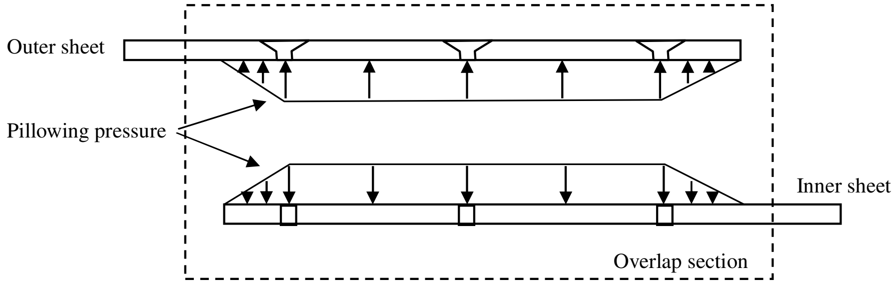

b) Tapered pillowing pressure applied to the faying surfaces of both the outer and inner sheets in the overlap sectionz

Fig. 7 Schematic presentations of the riveted lap joint and pillowing pressure after the riveting process stage in the finite element simulations (not to scale).

stress and the hole edge decreased from 1.94 to 1.28 mm, when the large clearance fit from the 0.06 to 0.18 mm was used. This finding strongly suggests that the fatigue strength of lap joints with large clearance fits would be significantly reduced, which is consistent with available experimental results [20,21].

In the study of the effect of the friction coefficient on the stress state in joints, a clearance fit of the 0.06 mm was used for all the FE models. From Fig. 8d, it can be seen that the friction coefficient had a certain impact on the edge stress. However, the magnitude and location of the peak tensile hoop stress was not affected by the friction coefficient. The hole edge and peak hoop stresses were approximately −69.2 and 205.9 MPa for the joint with the 0.2 friction coefficient, −110.9 and 218.2 MPa for the joint with the 0.4 friction coefficient, and −134.1 and 218.8 MPa for the joint with the 0.6 friction coefficient. For aging aircraft due to the existence of heavy fretting damage, the contact surface becomes coarser and thus

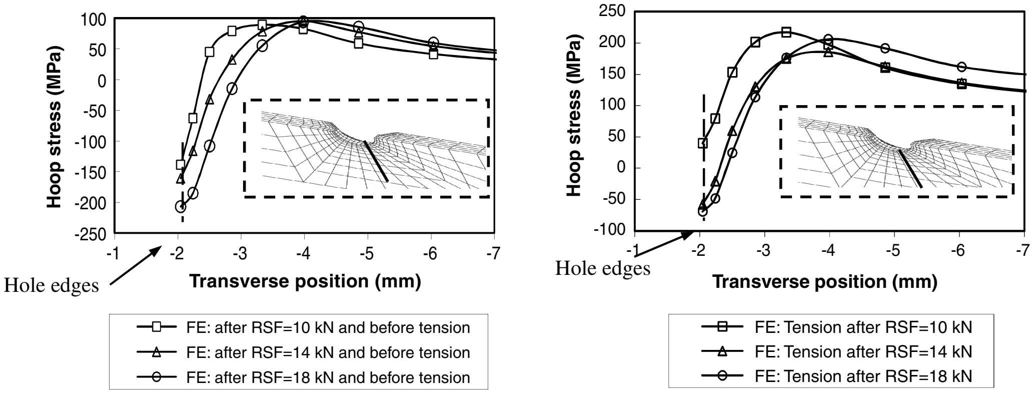

a) Residual hoop stress after riveting **b) Effect of rivet squeeze force (in tension)**

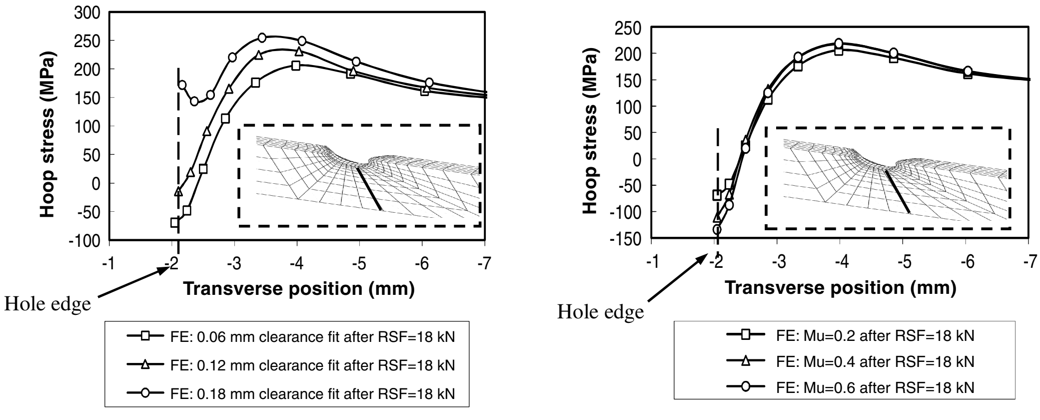

c) Effect of clearance fit (in tension) **d) Effect of friction coefficient (in tension)**

Fig. 8 Variations in the hoop stress along the transverse path at the top-row fastener on the outer-sheet faying surface under different conditions.

Table 8 Increment in the hoop (longitudinal) stress compared with the joint with the 0.06 mm clearance fit when the 18 kN riveted joints are loaded in tension up to 98.6 MPa

Clearance fit, mm	Stress at hole edge, MPa	Increment at hole edge, %	Maximum stress in hole vicinity, MPa	Distance to hole edge, mm	Increment of maximum stress, %
0.06	−69.2	0	205.9	1.94	0
0.12	−14.5	+79	231.3	1.93	+12
0.18	172	+349%	254.6	1.28	+24

the friction coefficient would increase and is assumed to be greater than the initial 0.2 value.

2. *Variations in the Contact and Friction Stresses*

Variations in the contact and friction stresses along the joint axial (longitudinal) path on the faying surface of the outer sheet were examined, and the results are presented in Fig. 9. The following can be seen:

1) The contact stress was only distributed in a very small region in the hole vicinity, and the largest stress was located at the hole edge.

2) A large friction coefficient generated a large contact stress, the maximum contact stress being approximately 300 MPa for the 0.2 friction coefficient, 360 MPa for the 0.4 friction coefficient, and 390 MPa for the 0.6 friction coefficient after the riveting process (Fig. 9a).

3) The contact stress increased, especially for the 0.2 friction coefficient case (Fig. 9b), when the joints were loaded to a remote tensile stress of 98.6 MPa.

4) The magnitude of the friction stress was much lower than the contact stress (Fig. 9c). The difference between the friction and contact stresses could be due to the relatively small movement that occurs between the inner and outer sheets. The maximum contact stress was different for all three holes when the joint was subjected to a remote tensile stress of 98.6 MPa. This extremely complicated loading situation involved the load transmission, secondary bending, contact among the rivets and sheets, friction between contact pairs, stress concentration at the existing hole, nonlinearities in both materials, and the geometric deformation conditions.

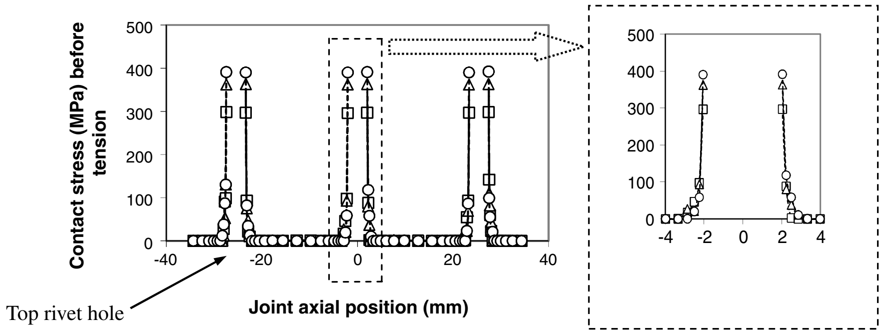

a) Riveted joints before tension

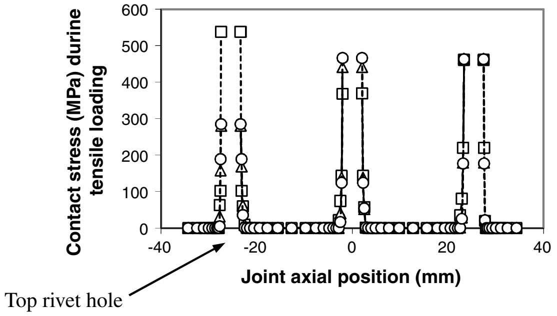

b) Joints loaded using the 98.6 MPa tensile stress

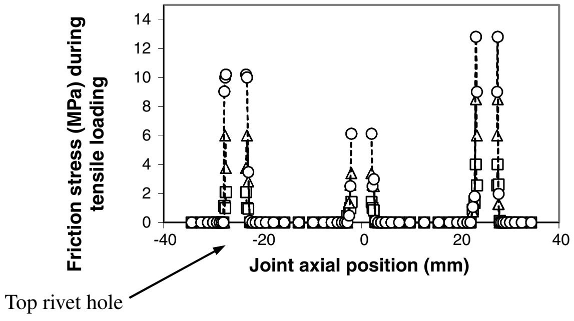

c) Friction stress with the joints loaded using the 98.6 MPa tensile stress

Fig. 9 Effects of friction coefficient on the contact and friction stresses along the joint axial position. The friction coefficients are 0.2 (□), 0.4 (△), and 0.6 (○) .

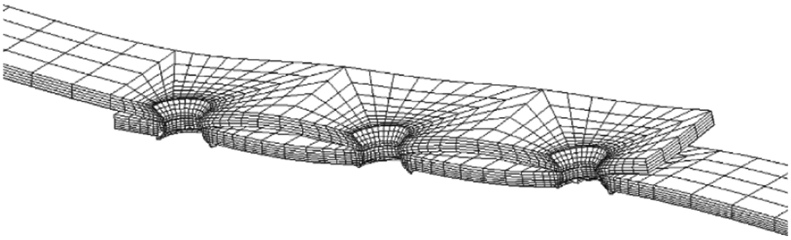

a) Joint over lap region deformation enlarged 10 times

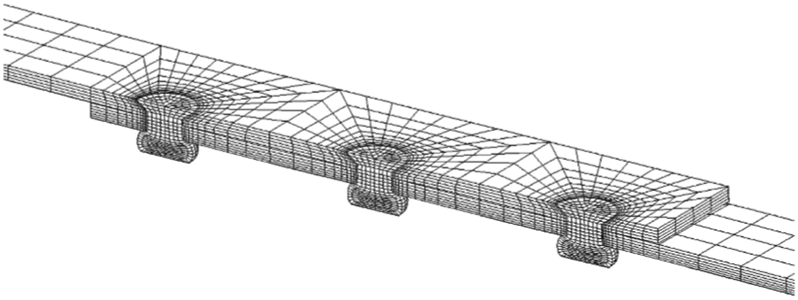

b) True deformation for the riveted lap joint riveted using the 18 kN squeeze force

Fig. 10 Deformation of the lap joint with the pillowing pressure of the PS4 = 1.296 MPa in pitch area and tapered in overlapped-edge areas for joint remote tensile stress of 98.6 MPa.

3. Corrosion-Pillowing Effect on the Hoop-Stress Variation

After the riveting process, internal pressure was applied to the faying surfaces to simulate corrosion pillowing. Pillowing deformation is the relative out-of-plane displacement between the two sheets. Limited impact of the RSF on the pillowing deformation was found from the numerical results, this deformation being dominated by the applied pillowing-pressure value. The overall joint lateral deformations in the overlap section during the tensile loading stage are shown in Fig. 10. Secondary bending occurred at the top-row rivet position in the outer sheet as well as the bottom-row rivet in the inner sheet near the overlap end. The maximum pillowing displacement occurred at the pitch center and is summarized in Table 9. Numerical results showed that the pillowing slightly decreased when the joint remote stress was applied. The pillowing deformation is, at most, 5% of the overlap thickness (2 × 1.6 mm) for all the analyzed pressure cases.

Crack nucleation usually first occurs in the top fastener-hole vicinity on the outer-sheet faying surface for the noncorroded-joint fatigue tests [7]. However, this may not be the case in the presence of corrosion pillowing. To assess the strength in the three fastener-hole regions, hoop-stress variation along three transverse paths, on both the outer- and inner-sheet faying surfaces were studied. These lines were located along the three rivet rows on each faying surface, perpendicular to the joint longitudinal tensile direction. Numerical results showed that a large RSF reduced the stress concentration at the hole edge and moved the peak tensile stress away. For clarity, only stress variations in the 18 kN RSF riveted joint, loaded in tension up to 98.6 MPa, are presented in Fig. 11. The following characteristics can be observed from the figure:

1) The peak tensile hoop stresses near the three hole edges in the inner sheet were smaller than in the corresponding outer sheet.

2) The top rivet hole in the outer sheet still had the highest tensile stress region when the pillowing stresses were small, within the range between PS0 = 0 and PS2 = 0.634 MPa.

3) Large corrosion-pillowing pressures of PS3 = 0.951 and PS4 = 1.269 MPa greatly increased the stress magnitudes at all rivet holes, especially at the middle hole, while decreasing the differences in the stress magnitudes among the three holes.

The middle hole region became a high-stress area, as the top hole region for the high-corrosion case of 1.269 MPa in the outer sheet. Hoop-stress increments caused by the high pillowing pressure to the 18 kN riveted joint in tension are summarized in Table 10 and compared with the 10 kN RSF riveted noncorroded joint (i.e., the PS0 = 0 pillowing-pressure condition). These results suggest that the pillowing pressure could significantly decrease the joint strength, and the outer sheet appears to be the weakest element, especially in both top- and middle-row hole regions.

C. Full-Field Stress Contours

The full-field stress distributions can provide insightful information to capture the peak stress level and the highly-stressed-area location. The maximum principal stress during the tensile loading stage is of great importance in the study of crack nucleation.

1. Effects of RSF, Clearance Fit, and Friction Coefficient

Effect of RSF on the maximum principal stress is presented elsewhere [17]. A high rivet squeeze force moved the high-stressed region away from the vicinity of the hole edge, and large maximum principal stress mainly occurred at the top-row rivet region. The large maximum-principal-stress distribution area and shape were consistent with experimental fatigue-testing results on noncorroded joints [7].

Table 9 Pillowing deformation predicted by the FE analysis

		Relative pillowing displacement,[a] mm	
Thickness loss, % [11]	Pillowing pressure, MPa[11]	Before tension	Remote tensile stress of 98.6 MPa
2.5	PS1 = 0.317	0.047	0.033
5	PS2 = 0.634	0.083	0.062
7.5	PS3 = 0.951	0.121	0.087
10	PS4 = 1.269	0.162	0.132

[a] At pitch center between the inner and outer sheets within the top- and middle-row rivets.

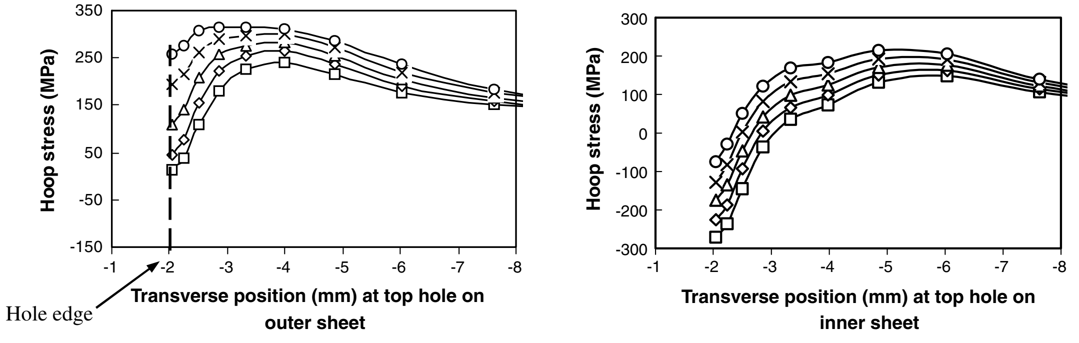

a) Top hole position

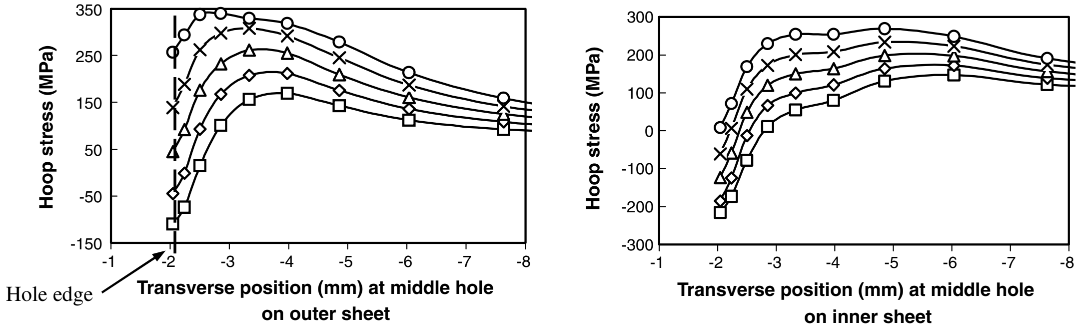

b) Middle hole position

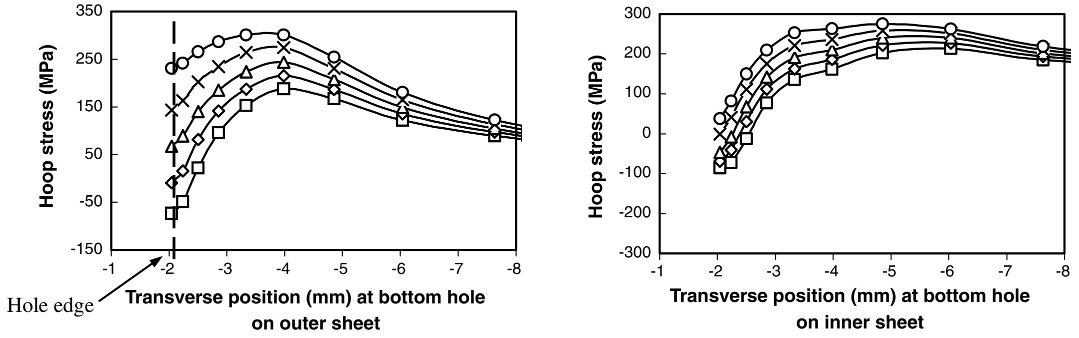

c) Bottom hole position

Fig. 11 Hoop-stress variations along the three transverse paths for remote tensile stress of 98.6 MPa. The lap joints were riveted using the 18 kN force and different pillowing pressures (□: PS0 = 0, ◇: PS1 = 0.317, △: PS2 = 0.634, ×: PS3 = 0.951, and ○: PS4 = 1.269 MPa).

Effects of clearance fit on the maximum-principal-stress condition on the outer-sheet faying surface is shown in Fig. 12, with the 18 kN RSF riveted lap joints loaded to a remote tensile stress of 98.6 MPa. The 0.2 friction coefficient was used in the Coulomb friction law for this effect assessment. The peak maximum principal stress in the top-row rivet region considerably increased with the increment in the clearance fit, which intersected the top fastener hole for both the 0.12 and 0.18 mm clearance-fit conditions. This intersection occurred at approximately 45° for the 0.12 mm clearance-fit joint and near 90° for the 0.18 mm clearance-fit joint, relative to the joint longitudinal tensile direction. Similar intersection location and degree of the stress increment were observed for the middle hole.

Table 10 Hoop-stress increment in the outer sheet when loaded in tension up to 98.6 MPa

Joint	Pillowing pressure	Stress at hole edge, MPa	Increment at hole edge, %	Peak stress in hole vicinity	Distance of peak stress to hole edge, mm	Increment of peak stress, %
			Top rivet-hole region			
10 kN riveted noncorroded joint	PS0	116.9	0	246.1	1.29	0
18 kN riveted joint	PS2	110.4	−5.6	284.5	1.94	+15.6
18 kN riveted joint	PS3	192.5	+64.7	311.0	1.29	+26.4
18 kN riveted joint	PS4	257.9	+120.6	315.4	0.81	+28.2
			Middle rivet-hole region			
18 kN RSF riveted joint	PS2	44.4	−62.0	261.9	1.29	+6..4
18 kN RSF riveted joint	PS3	138.9	+18.8	307.8	1.29	+25.1
18 kN RSF riveted joint	PS4	257.2	+120.0	339.9	0.81	+38.1
			Bottom rivet-hole region			
18 kN RSF riveted joint	PS2	67.3	−42.4	242.9	1.94	−1.3
18 kN RSF riveted joint	PS3	142.8	+22.2	274.1	1.94	+11.4
18 kN RSF riveted joint	PS4	230.1	+96.8	300.6	1.94	+22.1

a) The joint with the 0.06 mm clearance fit

b) The joint with the 0.12 mm clearance fit

c) The joint with the 0.18 mm clearance fit

Fig. 12 Effects of clearance fit of the a) 0.06, b) 0.12, and c) 0.18 mm on the maximum principal stress (MPa) on the outer-sheet faying surface for the 18 kN RSF riveted joints were loaded to a remote tensile stress of 98.6 MPa using the 0.2 friction coefficient in the Coulomb friction law.

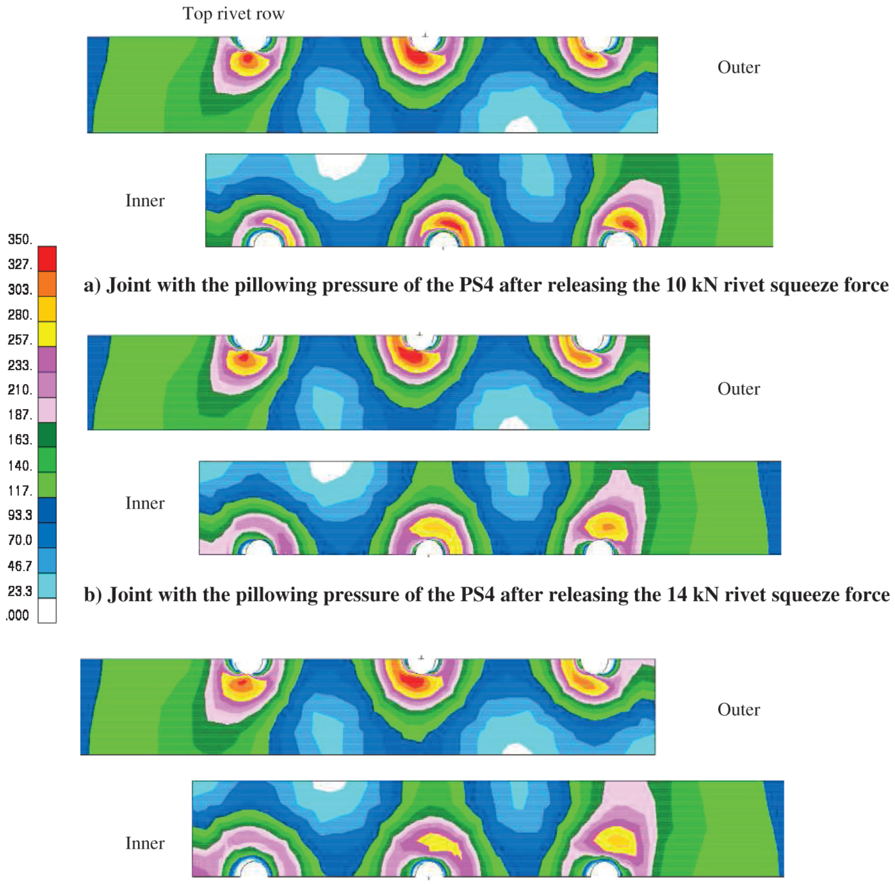

a) Joint with the pillowing pressure of the PS4 after releasing the 10 kN rivet squeeze force

b) Joint with the pillowing pressure of the PS4 after releasing the 14 kN rivet squeeze force

c) Joint with the pillowing pressure of the PS4 after releasing the 18 kN rivet squeeze force

Fig. 13 Maximum principal stress (in megapascals) on both the outer- and inner-sheet faying surfaces for a remote tensile stress of 98.6 MPa, as well as the PS4 = 1.296 MPa pillowing pressure within the overlap region.

A fatigue crack could originate at the location with the highest maximum principal stress for each clearance fit. Given the high stress combined with its higher distribution area for the 0.18 mm clearance fit, a crack would nucleate and grow more quickly than in the other joints. These crack-nucleation sites were also found experimentally [7,12,20,21], which may be explained, based on the current numerical results, by the presence of different clearance fits induced by the manufacturing process.

The full-field contours showing the maximum-principal-stress condition under the effect of the friction coefficient can be found in [22]. The peak stress and its area were slightly increased with increments of the friction coefficient in the vicinity of the top rivet-hole area.

2. *Corrosion Pillowing*

Both the outer- and inner-sheet faying surfaces were chosen for a clear investigation of this issue. The maximum principal stresses for joints loaded in tension of the 98.6 MPa stress, under the PS4 = 1.296 MPa corrosion-pillowing condition, are presented in Fig. 13. Comparing with Fig. 12a, it can be seen that the pillowing pressure significantly affected the stress condition by creating a tensile stress in the hole vicinity, especially at the middle hole region in the outer sheet, with a peak of approximately 350 MPa. This large highly stressed area is closer to the hole edges in the outer sheet than in the inner sheet. The corresponding stress magnitude at the top hole region was approximately 310 MPa, lower than the peak stress at the middle hole region. For comparison, the corresponding peak stresses were approximately 140 MPa at the middle hole and 250 MPa at the top hole regions of noncorroded joints [17], meaning that the corresponding increases in the maximum-principal-stress magnitudes compared with the noncorroded joints were approximately 150% at the middle hole and 24% at the top hole regions for the PS4 = 1.296 MPa pillowing pressure. If comparing the highest peak stress only, the corresponding stress increase was approximately 40% in the highly corroded joints (350 versus 250 MPa). Because of the corrosion-pillowing effect, the maximum principal stress and its area increased not only at the top rivet-hole region, but also at the middle and, to a lesser degree, in the bottom rivet holes. The strength of the outer sheet was decreased more than that of the inner sheet, because both the stress magnitude and large stress area in the former were greater than in the latter. The middle hole region had the largest peak stress area for the outer sheet for PS4 = 1.296 MPa. The rivet squeeze force had limited effect on the magnitude of maximum principal stress and its area size in the hole vicinity of the outer sheet, the weak element. Thus, areas in the vicinities of both the top and middle holes of the outer sheet would become the potential sites for an easy multiple-site crack nucleation. The fatigue strength of the lap joints affected by severe corrosion would be significantly decreased, which is consistent with existing experimental results [8–12]. The obtained stress condition information could greatly help us to understand the impact degree on the aged joint structures from the corrosion pillowing.

V. Conclusions

Both experimental and numerical studies of lap joints with three-row countersunk rivets were carried out. In situ strain values were measured using microstrain gauges during the entire loading sequence. Good agreement was achieved between the experimental results and 3-D FE predictions in the rivet driven-head deformations induced by the riveting process and strain variations during the entire loading sequence.

The empirical regression expression, obtained from tests, could accurately predict the rivet driven-head deformation for the MS20426ADx-x-type rivet using the force-controlled riveting method.

The (longitudinal) hoop-stress variations along the transverse path in the top rivet-hole region on the outer-sheet faying surface were assessed. A large clearance fit could significantly increase both the hole-edge hoop stress and the maximum hoop stress and would reduce the joint fatigue strength. The numerical results suggested that the clearance fit played a significant role in achieving a high fatigue strength in joints. Thus, the clearance-fit level must be taken into consideration for achieving high-fatigue-rated riveted lap joints.

Three possible crack-nucleation sites were predicted from the different clearance-fit models with the aid of the full-field maximum-principal-stress condition, which can be used to explain the obtained fatigue-test phenomenon from the noncorroded lap joints.

High contact stress was induced by the riveting process, while the friction stress was much smaller than the contact stress. Both the contact and friction stresses were located in very small areas in the fastener-hole vicinities.

Corrosion pillowing significantly increases the stress magnitude in the three fastener-hole vicinities and would definitely lead to the occurrence of multiple-site-damage areas in corroded lap joints, while only the top-row rivet area is the high-stress area in the noncorroded lap joints. When the introduced pillowing pressure was larger than PS2 (5% thickness loss), the highest-stress area was located at the middle-row rivet area. The rivet squeeze force had limited effect on the stress magnitude, as well as the high-stress-area size. The multiple-site damage would greatly decrease the integrity of the lap joint. This study shows that to safely operate aged aircraft, it is extremely important to accurately detect corrosion conditions in joint structures and to repair the highly corroded parts in time.

Acknowledgments

The financial assistance received from the Department of National Defence and Defence Research and Development—Canada is gratefully acknowledged. This work was also partially supported by the Institute for Aerospace Research (IAR) and AP/ES, Inc., collaboration on fretting fatigue. This work has been carried out under IAR Program 303, “Aerospace Structures, the Short Crack Model Development.” Our sincere acknowledgements to J. P. Komorowski and G. Eastaugh for their valuable discussions, suggestions, and help in the research. Many thanks to those people who have contributed to the work in one way or another.

References

[1] Müller, R. P. G., “An Experimental and Analytical Investigation on the Fatigue Behavior of Fuselage Riveted Lap Joints,” Ph.D. Thesis, Delft Univ. of Technology, Delft, The Netherlands, Oct. 1995.

[2] Fung, C-P., and Smart, J., “Riveted Single-Lap Joints. Part 1: A Numerical Parametric Study,” *Proceedings of the Institution of Mechanical Engineers, Part G (Journal of Aerospace Engineering)*, Vol. 211, No. 1, 1997, pp. 13–27.
doi:10.1243/0954410971532460

[3] Markiewicz, E., Langrand, B., Deleotombe, E., Drazetic, P., and Patronelli, L., “Analysis of the Riveting Forming Mechanisms,” *International Journal of Materials and Product Technology*, Vol. 13, Nos. 3–6, 1998, pp. 123–145.
doi:10.1504/IJMPT.1998.036232

[4] Szolwinski, M. P., and Farris, T. N., “Linking Riveting Process Parameters to the Fatigue Performance of Riveted Aircraft Structures,” *Journal of Aircraft*, Vol. 37, No. 1, 2000, pp. 130–137.
doi:10.2514/2.2572

[5] Trego, A., and Cope, D., “Evaluation of Damage Tolerance Analysis Tools for Lap Joints,” *AIAA Journal*, Vol. 39, No. 12, 2001, pp. 2250–2254.
doi:10.2514/2.1256

[6] Mackerle, J., “Finite Element Analysis of Fastening and Joining: A Bibliography (1990–2002),” *International Journal of Pressure Vessels and Piping*, Vol. 80, No. 4, 2003, pp. 253–271.
doi:10.1016/S0308-0161(03)00030-9

[7] Eastaugh, G. F., Straznicky, P. V., Krizan, D. V., Merati, A. A., and Cook, J., “Experimental Study of the Effects of Corrosion on the Fatigue Durability and Crack Growth Characteristics of Longitudinal Fuselage Splices,” *Proceedings of the 4th DoD/FAA/NASA Aging Aircraft Conference*, St. Louis, MO, 15–18 May 2000.

[8] Bellinger, N.C., Komorowski, J. P., and Benak, T. J., “Residual Life Predictions of Corroded Fuselage Lap Joints,” *International Journal of Fatigue*, Vol. 23, No. S1, 2001, pp. 349–356.
doi:10.1016/S0142-1123(01)00148-7

[9] Bellinger, N.C., Krishnakumar, S., and Komorowski, J. P., “Modelling of Pillowing Due to Corrosion in Fuselage Lap Joints,” *Canadian*

Aeronautics and Space Journal, Vol. 40, No. 3, 1994, pp. 125–130.

[10] Bellinger, N.C., and Komorowski, J. P., “Corrosion Pillowing Stresses in Fuselage Lap Joints,” *AIAA Journal*, Vol. 35, No. 2, 1997, pp. 317–320.
doi:10.2514/2.94

[11] Bellinger, N.C., Komorowski, J.P., and Gould, R. W., “Damage Tolerance Implications of Corrosion Pillowing on Fuselage Lap Joints,” *Journal of Aircraft*, Vol. 35, No. 3, 1998, pp. 487–491.
doi:10.2514/2.2322

[12] Bellinger, N. C., Komorowski, J. P., and Gould, R. W., “Corrosion Pillowing in Aircraft Fuselage Lap Joints,” *Journal of Aircraft*, Vol. 44, No. 3, 2007, pp. 758–763.
doi:10.2514/1.18589

[13] Li, G., and Shi, G., “Investigation of Residual Stress in Riveted Lap Joints: Experimental Study,” Institute for Aerospace Research, National Research Council Canada, Rept. LTR-SMPL-2003-0099, 2003.

[14] Li, G., and Shi, G., “Effect of the Riveting Process on the Residual Stress in Fuselage Lap Joints,” *Canadian Aeronautics and Space Journal*, Vol. 50, No. 2, 2004, pp. 91–105.

[15] Li, G., Shi, G., and Bellinger, N. C., “Studies of Residual Strain in Lap Joints,” *Journal of Aircraft*, Vol. 43, No. 4, 2006, pp. 1145–1151.
doi:10.2514/1.18125

[16] Li, G., Shi, G., and Bellinger, N.C., “Studies of Residual Stress in Single-Row Countersunk Riveted Lap Joints,” *Journal of Aircraft*, Vol. 43, No. 3, 2006, pp. 592–599.
doi:10.2514/1.18128

[17] Li, G., Shi, G., and Bellinger, N.C., “Residual Stress/Strain in Three-Row Countersunk Riveted Lap Joints,” *Journal of Aircraft*, Vol. 44, No. 4, 2007, pp. 1275–1285.
doi:10.2514/1.26748

[18] *MARC® Volume B: Element Library, Version K7*, MARC Analysis Research Corp., Palo Alto, CA, 1997.

[19] “Metallic Material and Elements for Aerospace Vehicle Structures,” U.S. Department of Defense, MIL-HDBK-5H, Dec. 1998.

[20] Eastaugh, G. F., Simpson, D. L., Straznicky, P. V., and Wakeman, R. B., “A Special Uniaxial Coupon Test Specimen for the Simulation of Multiple Site Fatigue Crack Growth and Linkup in Fuselage Skin Splices,” AGARD, AGARD-CP-568, Neuilly-sur-seine, France, Dec. 1995.

[21] Vlieger, H., and Ottens, H. H., “Uniaxial and Biaxial Tests on Riveted Fuselage Lap Joint Specimens,” U.S. Department of Transportation and Federal Aviation Administration, Rept. DOT/FAA/AR-98/33, Washington, D.C., 1998.

[22] Li, G., Shi, G., and Bellinger, N. C., “Effects of Fastener Clearance Fit And Friction Coefficient on the Stress Condition in Triple-Row Riveted Lap Joints,” 51st AIAA/ASME/ASCE/AHS/ASC Structures, Structural Dynamics, and Materials Conference, AIAA Paper 2010-3025, Orlando, FL, 12–15 April 2010.